Incoherent ultrafast energy transfer in phycocyanin 620 from *Thermosynechococcus vulcanus* revealed by polarization-controlled two dimensional electronic spectroscopy ⊘

Jiayu Wang ; Ruidan Zhu ; Jiading Zou ; Heyuan Liu ; Hanting Meng ; Zhanghe Zhen; Wenjun Li; Zhuan Wang ; Hailong Chen ; Yang Pu ✉ ; Yuxiang Weng ✉

View Online

Export Citation

Incoherent ultrafast energy transfer in phycocyanin 620 from *Thermosynechococcus vulcanus* revealed by polarization-controlled two dimensional electronic spectroscopy

Jiayu Wang,[1,2] (iD) Ruidan Zhu,[1] (iD) Jiading Zou,[3] (iD) Heyuan Liu,[1,2] (iD) Hanting Meng,[1,2] (iD) Zhanghe Zhen,[1] Wenjun Li,[4] Zhuan Wang,[1] (iD) Hailong Chen,[1,2,3] (iD) Yang Pu,[5,a)] (iD) and Yuxiang Weng[1,2,3,a)] (iD)

AFFILIATIONS

[1] Laboratory of Soft Matter Physics, Institute of Physics, Chinese Academy of Sciences, Beijing 100190, People's Republic of China
[2] University of Chinese Academy of Sciences, Beijing 100049, People's Republic of China
[3] Songshan Lake Materials Laboratory, Dongguan 523808, Guangdong, People's Republic of China
[4] Yantai Institute of Coastal Zone Research, Chinese Academy of Sciences, Yantai 264003, People's Republic of China
[5] School of Agriculture, Ludong University, Yantai 264025, People's Republic of China

[a)] Authors to whom correspondence should be addressed: ypu@ldu.edu.cn and yxweng@iphy.ac.cn

ABSTRACT

Phycocyanin 620 (PC_{620}) is the outermost light-harvesting complex in phycobilisome of cyanobacteria, engaged in light collection and energy transfer to the core antenna, allophycocyanin. Recently, long-lived exciton–vibrational coherences have been observed in allophycocyanin, accounting for the coherent energy transfer [Zhu *et al.*, Nat. Commun. **15**, 3171 (2024)]. PC_{620} has a nearly identical spatial location of three α84–β84 phycocyanobilin pigment pairs to those in allophycocyanin, inferring an existence of possible coherent energy transfer pathways. However, whether PC_{620} undergoes coherent or incoherent energy transfer remains debated. Furthermore, accurate determination of energy transfer rates in PC_{620} is still necessary owing to the spectral overlap and broadening in conventional time-resolved spectroscopic measurements. In this work, the energy transfer process within PC_{620} was directly resolved by polarization-controlled two dimensional electronic spectroscopy (2DES) and global analysis. The results show that the energy transfer from α84 to the adjacent β84 has a lifetime constant of 400 fs, from β155 to β84 of 6–8 ps, and from β155 to α84 of 66 ps, fully conforming to the Förster resonance energy transfer mechanism. The circular dichroism spectrum also reveals that the α84–β84 pigment pair does not form excitonic dimer, and the observed oscillatory signals are confirmed to be vibrational coherence, excluding the exciton–vibrational coupling. Nodal line slope analysis of 2DES further reveals that all the vibrational modes participate in the energy dissipation of the excited states. Our results consolidate that the ultrafast energy transfer process in PC_{620} is incoherent, where the twisted conformation of α84 is suggested as the main cause for preventing the formation of α84–β84 excitonic dimer in contrast to allophycocyanin.

Published under an exclusive license by AIP Publishing. https://doi.org/10.1063/5.0222587

I. INTRODUCTION

Photosynthesis is one of the most important energy conversion processes on the earth.[1] Light harvesting complexes are important functional units for photosynthesis. They are responsible for light absorption and subsequent excitation energy transfer (EET) to a reaction center.[2] An efficient EET process is critical for the success of photosynthesis. Cyanobacteria are one of the most important photosynthetic organisms and are responsible for producing ∼25% of global oxygen.[3,4] The main light-harvesting complex in cyanobacteria is the phycobilisome (PBS) complex, including phycocyanin (PC) rods and allophycocyanin (APC) cores. Early studies on PBS have shown that the EET process is dominated by the Förster resonance energy transfer (FRET) mechanism.[5,6] It assumes energy hopping over the pigments arranged sparsely in incoherent form and occurs on femtosecond to picosecond time scales.[7,8] In recent

years, the quantum coherent EET mechanism has been proposed to account for the near unity efficiency in the EET process.[9] It manifests as oscillatory signals on the EET kinetics detected in a variety of light harvesting systems in ultrafast spectroscopic measurements.[10–14] Quantum coherences can be classified as electronic, vibrational, and vibronic coherences.[15] Fragile electronic coherences and vibrational coherences originating from a single monomer limit their role in the coherent EET process,[13,16] whereas the coupling between the excitonic and vibrational degrees of freedom facilitates the energy delocalization across different pigments, further enhancing the EET rate and efficiency.[15,17–19] To realize the coherent EET, the quantum coherences should have a long enough lifetime to match the time scale of EET. Recently, we have found that exciton–vibrational coupling in the excitonic dimer can extend the coherence time significantly in the APC trimer via the quantum phase synchronization mechanism.[20] Explicitly, after photoexcitation, the anti-symmetric resonant vibrational collective modes of the dimer are coupled to the excitonic states of fast dephasing, leading to the fast energy dissipation of the anti-symmetric vibrational collective modes, and the decoupled symmetric collective modes of less energy dissipation survive. Thus, quantum phase synchronization provides a mechanism for the protection of exciton–vibrational coherences against the environmental noises at room temperature.

PC$_{620}$ from *Thermosynechococcus Vulcanus (T. vulcanus)* is the main light harvesting antenna in the PC rod, which is responsible for light harvesting and EET to APC. The location of PC$_{620}$ in PBS, together with the crystal structure of PC$_{620}$, is shown in Figs. 1(a) and 1(b). The EET pathways in PC$_{620}$ and PBS have been intensively investigated by time-resolved optical spectroscopy.[21–25] An ultrafast energy transfer process at ~500 fs revealed by the transient absorption (TA) anisotropy experiment was attributed to EET from $\alpha 84$ to $\beta 84$ located in adjacent monomers of PC$_{620}$.[5] The EET lifetime from $\beta 155$ to $\beta 84$ in a single monomer of PC$_{620}$ was estimated to be 50 ps by Debreczeny and Sauer under the FRET mechanism,[26,27] and this process was determined to be around 17 ps in the latest experiment inside PBS.[25] These lifetime constants were much longer than those from subsequent TA experiments on PBS, in which the lifetime constants for energy flow along the PC rod were determined to be around 1–10 ps and the energy equilibration among PC$_{620}$ hexamers completed within 3 ps.[23–25,28,29] In addition, the overall EET rate is faster in thermophilic cyanobacteria than that in other species of cyanobacteria owing to the assistance of the linker proteins in the former.[30] These findings suggest that the EET process within the PC$_{620}$ monomer should be faster than the reported 50 ps. Thus, an accurate experimental determination of the EET lifetime in PC$_{620}$ is necessary. Moreover, whether the ultrafast EET process is assisted by the exciton–vibrational coherence, that is, via coherent energy transfer, also needs further exploration. PC$_{620}$ shares a nearly identical structure of $\alpha 84$–$\beta 84$ dimer with APC, including the comparable intermolecular distance (21 Å), the analogous angles between transition dipoles (55°), as well as the same calculated intermolecular couplings (150 cm^{-1}).[31–33] Our recent work has experimentally confirmed the exciton–vibrational coherence in the $\alpha 84$–$\beta 84$ dimer in APC.[20] We noted that Beck *et al.* investigated the electronic coherence between the two exitonic states of $\alpha 84$–$\beta 84$ dimer in APC earlier in 1990s using various femtosecond time-resolved spectroscopic methods, such as two-color pump–probe anisotropy decay, stimulated photon-echo, and transient-grating

experiments.[34–37] Exciton electronic structure and solvation dynamics were thoroughly investigated, e.g., they observed a 10–30 fs decay component that was assigned to the interference between Feynman paths involving two exciton states, which has been recently confirmed as the electronic dephasing time with two dimensional electronic spectroscopy (2DES).[20] As to PC$_{620}$, previous spectral simulations indicated that the EET process in PC$_{620}$ is in incoherent form.[38,39] Therefore, whether the EET process in PC$_{620}$ is incoherent or coherent needs to be scrutinized by more sensitive spectroscopic methods.

In this work, we revisited the EET kinetics and vibronic effects within PC$_{620}$ using broadband 2DES, heterodyne-detected transient grating (HD-TG), broadband TA (BBTA) spectroscopy, and polarization-controlled 2DES at room temperature. 2DES is a powerful experimental tool for monitoring the EET process, intra- and intermolecular interactions, and energy dissipation mechanisms.[40–43] The projection of the spectra onto the excitation frequency (ω_1) and emission frequency (ω_3) enables 2DES a better spectral resolution for the congested conventional spectra. In addition, 2DES also boasts a high temporal resolution and a capability for the detection of quantum coherences. The quantum coherence beating signals in 2DES detection originate from the superpositions of quantum states created by the ultrafast laser pulses with a broad spectral bandwidth. Through performing Fourier transform (FT) analysis of the oscillation signals over the waiting time (T), the coherent frequencies can be extracted. We also utilized HD-TG spectroscopy and BBTA spectroscopy, which require much less acquisition time, to confirm the coherent signals.[14,44] However, even for 2DES, when the spectral broadening and overlap are severe, the cross-peaks in 2DES, a typical feature for energy transfer, are obscured by the main diagonal peaks, leading to the failure in the unambiguous identification of the EET process. To suppress the interference from the spectral broadening of the diagonal peaks, we eliminated the dominant population state signals, which are the source of spectral overlap and broadening, and highlighted the cross-peak features by using polarization-controlled 2DES reported by Zigmantas and co-workers.[45,46] By conducting experiments at parallel polarization $S_{\parallel} = (0°, 0°, 0°, 0°)$ and perpendicular polarization $S_{\perp} = (90°, 90°, 0°, 0°)$, the polarization-associated-spectra (PAS) can be derived as follows:[46,47]

$$S_Z = \frac{1}{3}\left(S_{\parallel} + 2S_{\perp}\right)\left(5\frac{S_{\parallel} - S_{\perp}}{S_{\parallel} + 2S_{\perp}} + 1\right),$$
$$S_Y = \frac{1}{3}\left(S_{\parallel} + 2S_{\perp}\right)\left(2 - 5\frac{S_{\parallel} - S_{\perp}}{S_{\parallel} + 2S_{\perp}}\right). \tag{1}$$

Thus, the 2D spectrum is separated into two components, with parallel (S_Z) and perpendicular (S_Y) polarizations relative to the polarization of the "pumped" transition. In S_Y, the signals at cross-peaks with large projection angles are notably enhanced, while the signals from interactions with parallel transition dipole moments are suppressed. This selective enhancement and suppression strategically eliminate the predominant population state signals, thereby highlighting the cross-peaks indicative of EET. By utilizing polarization-controlled 2DES, we directly measured the EET process from $\alpha 84$ to $\beta 84$ with a lifetime of 400 fs and from $\beta 155$ to $\beta 84$ with a lifetime of 6.6 ps at the cross-peaks, which were also consolidated by the ultrafast transient fluorescence experiment. These EET rates are
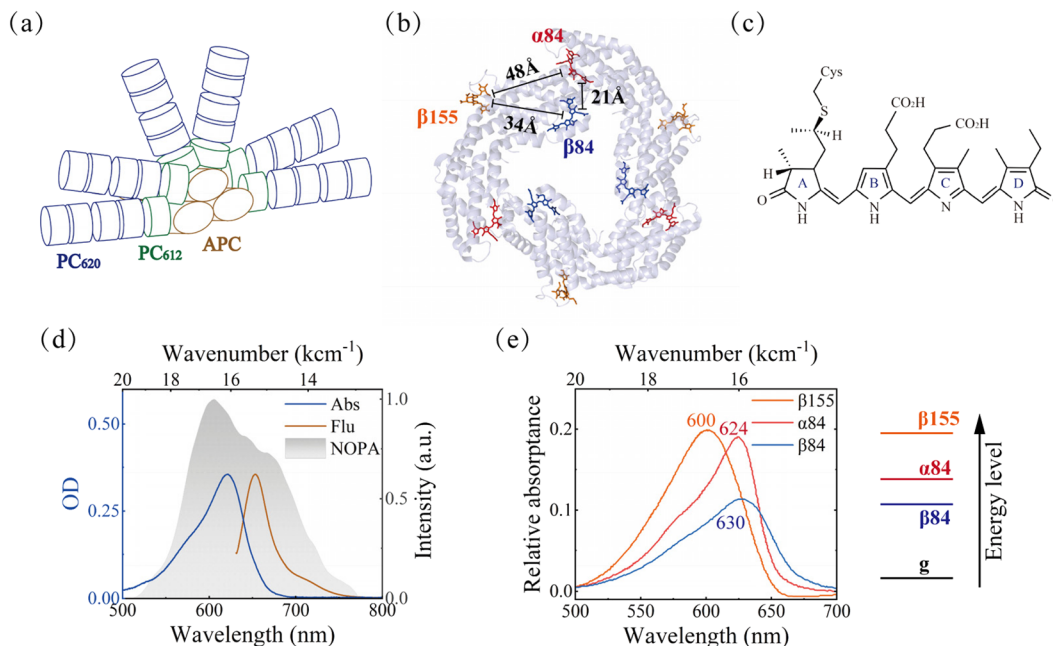
FIG. 1. (a) Model for the phycobilisome, with hexametric PC_{620} and trimeric PC_{612} disks in the rods and APC disks in the core.[32] (b) The x-ray structure of the PC_{620} trimer with the β84 (blue), β155 (orange), and α84 (red) PCB pigments (PDB ID code 1I7Y). (c) Structure of the phycocyanobilin chromophores. The four pyrrole rings are labeled A–D with the A ring linked to the phycobiliprotein structure by a cysteine (Cys) residue. (d) The absorption spectrum (blue) and the fluorescence spectrum (orange) of the PC_{620} hexamer at room temperature and the broadband spectral profile of the excitation laser pulses (shaded in gray). (e) Linear absorption spectra of β155 (orange), α84 (red), and β84 (blue) in monomeric PC at room temperature. Reprinted with permission from Debreczeny *et al.*, J. Phys. Chem. **97**, 9852 (1993). Copyright (1993) American Chemical Society. The energy level diagram of the three pigments is plotted on the right.

faster than that predicted by the FRET mechanism and matched better with the EET process in PBS. Meanwhile, distinct coherent signals were observed in the kinetics and Fourier transform yields the same coherence frequencies in 2DES, HD-TG, and BBTA. Through comparing the FT coherence map patterns predicted by theoretical models with those extracted from 2DES experiments, and by conducting time–frequency analysis to obtain the lifetimes of wavepackets from both excited-state and ground-state, we confirm that all the oscillatory signals originate from the pure vibrational coherence of phycocyanobilin (PCB) pigments. In addition, by exploring the solvation effect via nodal line slope analysis in 2DES, we find that PC_{620} exhibits an ultrafast solvation response, with vibrational modes actively engaged in the energy dissipation process. Our results confirm the absence of exciton–vibrational coupling states in the α84–β84 dimer and the EET process is dominated by an incoherent mechanism.

II. METHODS

A. Sample preparation

The extraction, isolation, and purification of PC_{620} from *T. vulcanus* are briefly described as follows. Cells of the *T. vulcanus* (NIES-2134) were grown in the BG11 medium at 39 °C. After 15 days, fresh algal cells were collected by centrifugation at 6000 rpm

for 20 min at 4 °C, and then, the precipitates were treated by liquid nitrogen grinding. Then, a 0.02M phosphate buffer solution (pH 6.9) was added to thaw algae cells at a mass to volume ratio of 1:10, the sample was centrifuged at 4 °C (12 000 rpm, 30 min), and the supernatant containing PC_{620} was obtained. The blue supernatant of PC_{620} crude extract was treated with 20% (w/v) ammonium sulfate for initial precipitation of impurities, which can be removed by centrifugation. In addition, most PC_{620} from the supernatant was precipitated by further increasing ammonium sulfate to 50% (w/v). A centrifuged deposit was dissolved in 0.02M phosphate buffer (pH 6.9) and was filtered through a cellulose acetate membrane (0.22 μm) for subsequent fast protein liquid chromatography (FPLC) purification. PC_{620} was further purified using an FPLC instrument equipped with a Butyl-S Sepharose 6 Fast Flow column. Finally, analytical grade PC_{620} (Abs_{620}/Abs_{280} = 5.3) was eluted with gradient $(NH_4)_2SO_4$. Following SDS-PAGE, Coomassie brilliant blue staining revealed two bands at 19 and 21 kDa, corresponding to α and β subunits (PDB 3O18) (see Fig. S1 of the supplementary material). The purified PC_{620} was frozen in liquid nitrogen and stored at −80 °C prior to the experiments. For all experiments, the PC_{620} proteins were dissolved in a 750 mM phosphate buffer (pH 6.8) to an optical density (OD) at the band maximum (620 nm) of 0.3–0.4 in a 1-mm-thick fused silica cell. Absorption measurements before and after the 2D experiments confirmed that the degradation is relatively small and has a negligible impact on the subsequent data analysis.

B. Spectroscopy

2DES is a form of photon echo spectroscopy involving three identical pulses with a time sequence as τ, T, and t. The first pulse creates coherence between the ground states and excited states of the system. After a coherence time interval τ, the second pulse interacts with the system, and the system evolves to populations of ground states, populations of excited states, and coherence between different excited states. Then, the system undergoes a period of free evolution during the waiting time T, until the arrival of the third pulse. The third pulse reintroduces coherence between the ground and excited states. After a time, t, the emitted signal is detected by heterodyne interference with a local oscillator (LO). Fourier transformation of the conjugates of τ and t yields 2D data correlating excitation (ω_1) and emission (ω_3) frequencies. It enables the detailed monitoring of signal changes during T, providing a comprehensive view of the system's evolution. In addition, both electronic and vibrational coherences within the molecular system, often manifested as beating signals on the EET kinetics, can be thoroughly investigated.[43,48]

The setup used for 2DES experiments has been described in detail elsewhere,[49,50] while a brief description is given here. An 800 nm Ti:sapphire laser (Spitfire Ace, Spectra-Physics) at the 5 kHz repetition rate was used to pump a home-built non-collinear optical parametric amplifier (NOPA). The output pulses with a spectrum centered at 620 nm were compressed to 7.3 fs (Fig. S2 of the supplementary material) using a combination of a grating pair and a fused silica prism pair. Then, the laser beam was split into four phase-locked beams using two beam splitters (Layertec) constituting the non-collinear BOXCARS 2DES setup. Three pulses were focused on the sample to emit the third order 2DES signal, which was heterodyne detected by LO. Achromatic half-wave plates (Thorlabs) were used to achieve an independent polarization control for each beam. The polarization combinations involved in the 2DES experiment were (0°, 0°, 0°, 0°) and (90°, 90°, 0°, 0°), respectively. The coherence time (τ) between the first two pulses was scanned by a 1.35 fs step from −54 to 54 fs. The waiting time (T) of 2DES was scanned by an 8 fs step within a temporal region of 1.2 ps and then scanned at uneven intervals to 200 ps. An excitation energy of 1.2 nJ per pulse was used for all measurements with the spot size (100 × 100 μm^2) at the sample. The excitation energy density was ~15 $\mu J/cm^2$. 2DES data were averaged five times in two independent experiments to obtain a higher quality of coherent dynamics. Fourier transform along T was performed from 80 fs to 1.2 ps to avoid the overlapping pulse effect, and the actual frequency resolution along ω_T was ~28 cm^{-1}. After zero-padding, the ω_T resolution displayed in all FT spectra was ~2 cm^{-1}.

III. RESULTS AND DISCUSSION

A. Excitation energy transfer

The schematic structure of the PBS in *T. vulcanus* is shown in Fig. 1(a), with PC rods surrounding APC cores.[31,32] Two hexametric PC_{620}, a trimeric PC_{612}, and various linker proteins compose a PC rod. The PC_{620} hexamer comprises two trimers arranged face to face, which possess a threefold axis of symmetry. The three-dimensional x-ray structure of the PC_{620} trimer and the spatial distribution of PCB pigments are shown in Fig. 1(b). Each monomer comprises

three PCB pigments: α84 in the α-subunit and β155 and β84 in the β-subunit. The α84 and β84 PCB pigments are located on the inner areas, whereas β155 is located on the outer circumference of the protein. The closest chromophores in the PC_{620} hexamer, between β84 and α84 from adjacent monomers, are separated by a center-to-center distance of only 21 Å.[51,52] The closest pigments in a single monomer, β84 and β155, are separated by 34 Å, while β155 and α84 are separated by 48 Å.[51,52] The structure of the PCB bilin is shown in Fig. 1(c) with the detailed conformation shown in Fig. S3 of the supplementary material, where the schematic presentation compares the dihedral angles between the pyrrole rings of A to D in α84 and β84 for PC_{620} and APC, respectively. The conformation of a bilin is defined by the planes of its four pyrrole rings and the dihedral angles between rings, where the chain of pyrrole rings in α84 is more twisted for PC_{620} than that for APC, while the chain of pyrrole rings in β84 is quite similar for both the PC_{620} and the APC. It has been confirmed that the bilin conformation has a significant impact on its spectral properties in our previous investigation of PBS.[53] The structural differences of bilins in PC_{620} and APC thereby would account for a tendency toward localized electronic states in PC_{620} and delocalized electronic states across the dimeric pigments in APC. Womick also suggested the different conformation of α84 between APC and PC_{620} might give rise to the exciton electronic structure in APC but not in PC_{620}.[38,39] Our circular dichroism (CD) spectrum shown in Fig. S4 of the supplementary material indicates localized states in PC_{620}, since there is no excitonic splitting in the CD spectrum expected from the electronic interaction between the adjacent α84 and β84 PCB pair. The absorption and fluorescence spectra of PC_{620} are shown in Fig. 1(d) (blue and orange lines) and can be covered by the broadband spectra of the excitation pulses for the 2DES measurement [the shaded area in Fig. 1(d)]. The different conformations and different protein environments of the PCB assembly (β155, β84, and α84) render the individual PCB pigments with different spectral properties. Debreczeny *et al.* showed that in the PC_{620} monomer, the maximum absorption of the β155 and β84 cofactors' individual spectra fell between 600 and 602 nm and between 628 and 630 nm, respectively, and the α84 cofactor's absorption maximum was 624 nm, as shown in Fig. 1(e).[54]

1. Conventional 2DES measurement

First, we employed 2DES to investigate the ultrafast EET process among the pigments in the PC_{620} hexamer. The representative 2D spectra at all parallel polarization ($S_{\parallel}$) recorded at around T = 40 fs, 200 fs, 2, and 20 ps are plotted in Fig. 2(a). Ground-state bleaching (GSB, positive signal) and stimulated emission (SE, positive signal) of PCB pigments give rise to a broad and elongated line shape along the diagonal. A similar phenomenon of diagonal elongation has also been observed in other PBS complex.[25] The broad spectral profile is attributed to the spectral broadening and overlap of the three PCB pigments as shown in Fig. 1(e). Excited-state absorption (ESA) of PCB pigments contributes to the negative signals below the diagonal. Typically, cross-peaks in 2DES signify either the occurrence of the EET process or exciton coupling. Our CD spectrum (Fig. S4 of the supplementary material) excludes the exciton coupling in PC_{620}; thus, these cross-peaks only originate from the EET process. Monitoring the evolution of the magnitudes helps track excitation and relaxation pathways. Figure 2(b)
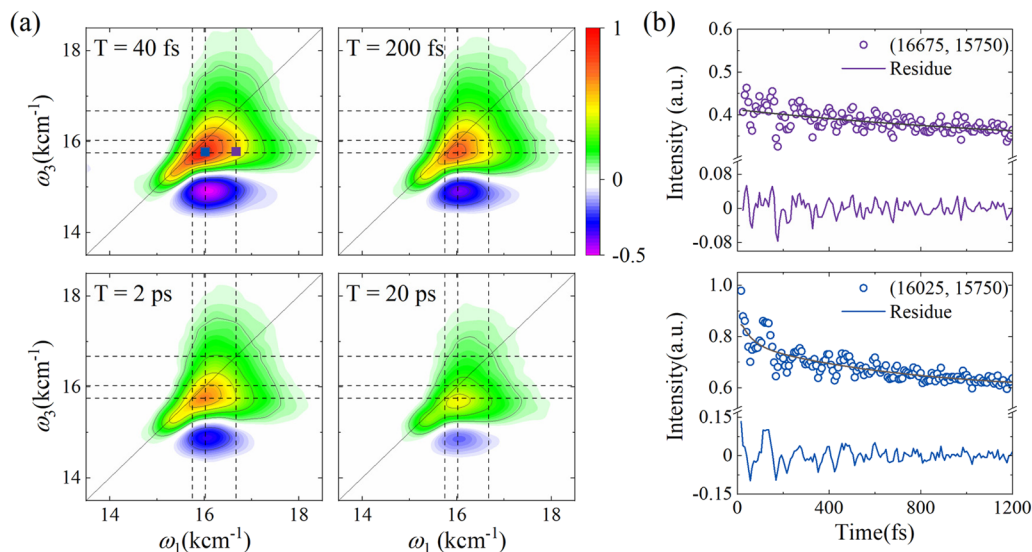
FIG. 2. (a) Pure absorptive 2D maps ($S_{||}$) of PC_{620} recorded at the waiting times of T = 40 fs, 200 fs, 2, and 20 ps with dashed lines indicating the excitonic energy levels. (b) The energy transfer kinetics (raw data in dots and single exponential fitting results in line) from 40 fs to 1.2 ps at the cross-peak (16 675, 15 750 cm^{-1}) and (16 025, 15 750 cm^{-1}) corresponding to the EET process from β155 to β84 and from α84 to β84, respectively. The color in the legend of (b) corresponds to the positions of peaks that are marked with squares with the same color in (a).

shows the kinetics at cross-peaks (16 675, 15 750 cm^{-1}) and (16 025, 15 750 cm^{-1}), which correspond to the EET process from α84 to β84 and from β155 to β84, respectively. We noted that these two kinetics at the cross-peaks all exhibit decay features instead of rising kinetics expected for the EET process; the reason for these unexpected results could be that the spectral broadening of the diagonal peaks overlaps and dominates the cross-peaks, leading to that the stronger population relaxation signals at the diagonal peaks obscure the weaker growing signals at the cross-peaks. Thus, the raw data of cross-peaks kinetics cannot reflect the true EET process.

To resolve the EET process from the raw data, we followed the general procedure for global analysis of the time-resolved 2D data from 40 fs to 200 ps.[55] From the three-exponential fitting of the 2D spectra, 2D decay-associated spectra (DAS) with lifetime constants of 447 fs, 8, and 54 ps, and a non-decay background indicated as "infinity," were obtained (Fig. S5 of the supplementary material). However, owing to the spectral broadening and the interference between the positive GSB and SE signals, and the negative ESA signals, assignment of the DAS to the individual pigments was impossible, hence the corresponding EET process. Then, we turned to analyze the extracted sliced spectra (T, ω_3) with excitation frequencies selected for the individual pigments at ω_1 = 16 675, 16 025, and 15 875 cm^{-1} from 2DES data as shown in Fig. S6 of the supplementary material. These selected excitation frequencies correspond to the maximum absorption of β155, α84, and β84. Although their absorption spectra are still partially overlapped, the weight of the excited-state population can be different. Then, we applied global analysis to these 1D spectra. The DAS for those 1D spectra at three different excitation wavelengths obtained by four-exponential

fitting are plotted in the left panels of Figs. 3(b)–3(d). According to previous research, the EET processes in PC_{620} mainly occur from α84 to β84 and from β155 to β84.[26] Based on the EET model with lifetime constants from global analysis as schematically shown in Fig. 3(a), the species-associated spectra (SAS) and the corresponding SAS-associated kinetics could be resolved. The SAS and the corresponding kinetics at the excitation frequency ω_1 = 16 675 cm^{-1} are shown in Fig. 3(b), which mainly excite β155. Based on the absorption peaks in SAS in comparison with those of β155, α84, and β84 in the steady-state absorption spectra shown in Fig. 1(e), the SAS component of 480 fs decay is similar to the absorption spectrum of α84 and can be assigned to the EET from α84 to β84. The SAS component of 8.6 ps decay is similar to the absorption spectrum of β155 and has a larger amplitude than the 480 fs component owing to a larger absorption coefficient of β155 than that of α84 at the excitation wavelength and is assigned to the EET from β155 to β84. The SAS of the 60 ps decay component and that of the fixed 3 ns rising component have similar spectral features, i.e., their positive signals only cover the absorptive spectrum of β84. Thus, the 60 ps decay component and the fixed 3 ns rising component are attributed to a faster and a slower relaxation process of the excited states of β84, respectively. In addition, the SAS and the corresponding kinetics at the excitation frequency of ω_1 = 16 025 cm^{-1} mainly exciting α84 are plotted in Fig. 3(c). Accordingly, the 460 fs decay component is assigned to EET from α84 to adjacent β84, while the 8 ps decay component is assigned to that from β155 to β84 and the 57 ps together with the fixed 3 ns component to the excited-state relaxation of β84. The SAS and the corresponding kinetics at excitation frequency ω_1 = 15 875 cm^{-1} are plotted in Fig. 3(d), which give rise to three decay components of 400 fs, 7.6, and 58 ps. The assignment of the EET
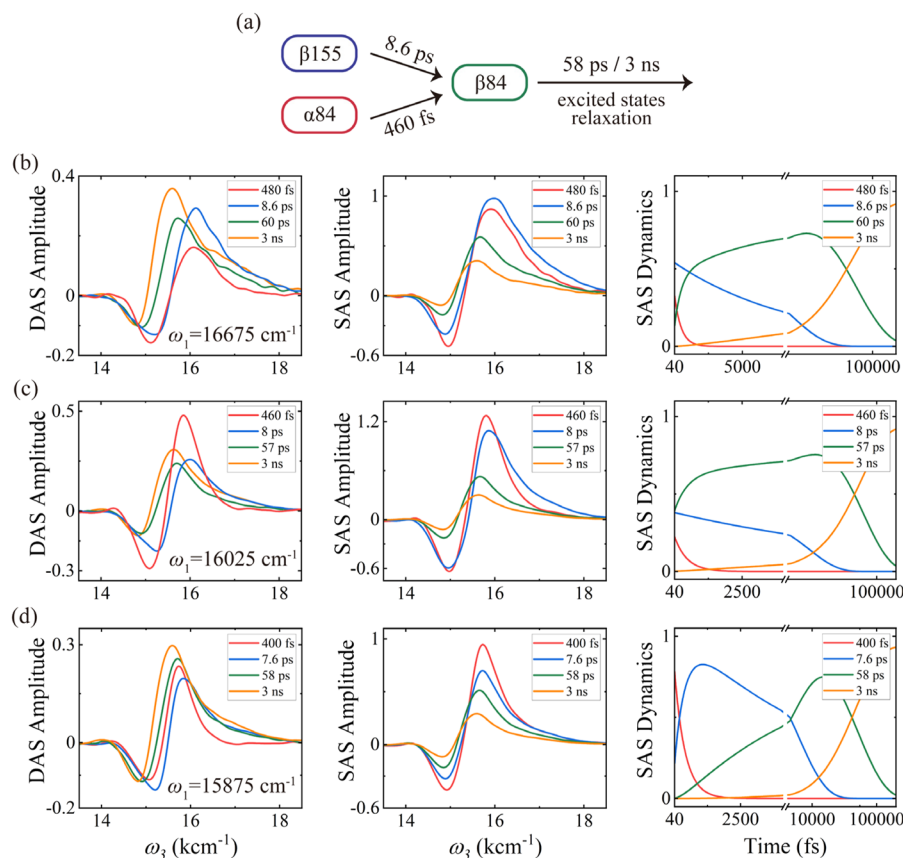
FIG. 3. (a) The EET model for global analysis. Global analysis of spectral evolution at typical excitation frequencies of 16 675 cm^{-1} (b), 16 025 cm^{-1} (c), and 15 875 cm^{-1} (d). Decay-associated spectra (DAS) (left panels) are obtained from a four-exponential fit of the sliced spectra from 40 fs to 200 ps. The species-associated emission spectra (SAS) (middle panels) and the corresponding kinetics (right panels) are resolved based on the DAS and the EET model. The corresponding lifetime constants are displayed in the upper-right corner in each panel.

processes is the same as those excited at 16 675 and 16 025 cm^{-1}. In addition, we also tried to resolve the EET from β155 to α84 with a larger separation of 48 Å. As detailed in S6 of the supplementary material, according to the FRET mechanism,[7]

$$k_{FRET}(r) = \frac{1}{\tau_D}\left(\frac{R}{r}\right)^6, \qquad (2)$$

where τ_D is the decay time of the donor in the absence of the acceptor, R is the Förster distance, and r is the distance between the donor and the acceptor, the EET lifetime constant is estimated to be 66 ps based on the distance between β155 and α84 with reference to the EET time constants for α84–β84 and β155–β84 pigment pairs and their separation distances. The fitting of the excited-state population decay kinetics for β155 at the peak (16 675, 16 675 cm^{-1}) in 2DES reveals three lifetime constants of the excited-state relaxation of β155, i.e., 905 fs, 8.8, and 66.7 ps (Fig. S7 and Table S1 of the supplementary material). The 905 fs component can be assigned to the protein-matrix solvation dynamics,[56,57] while 8.8 ps is assigned

to EET from β155 to β84 and 66.7 ps is assigned to EET from β155 to α84. This is in good agreement with the estimated value of 66 ps from FRET theory.

2. Polarization-controlled broadband 2DES

Then, to directly measure the EET process from the signals at cross-peaks by the elimination of spectral broadening effect, we conducted polarization-controlled broadband 2DES on PC$_{620}$. 2D spectra at perpendicular polarization (S$_\perp$) shown in Fig. S8 of the supplementary material show a similar signal distribution to S$_\parallel$, with major differences being the increment in signal intensity at cross-peaks at a longer waiting time. As depicted in Fig. S9 of the supplementary material, the signal intensity in S$_\perp$ at (16 675, 15 750 cm^{-1}) increases from 0 fs to 10 ps and the signal intensity at (16 025, 15 750 cm^{-1}) increases from 0 fs to 5 ps. We obtained polarization-associated-spectra (PAS) using Eq. (1). The representative S$_Y$ maps at T = 40 fs, 200 fs, 2, and 20 ps are displayed in Fig. 4(a), with the corresponding S$_Z$ maps shown in Fig. S10 of the supplementary material. The spectra of S$_Z$ nearly keep the same
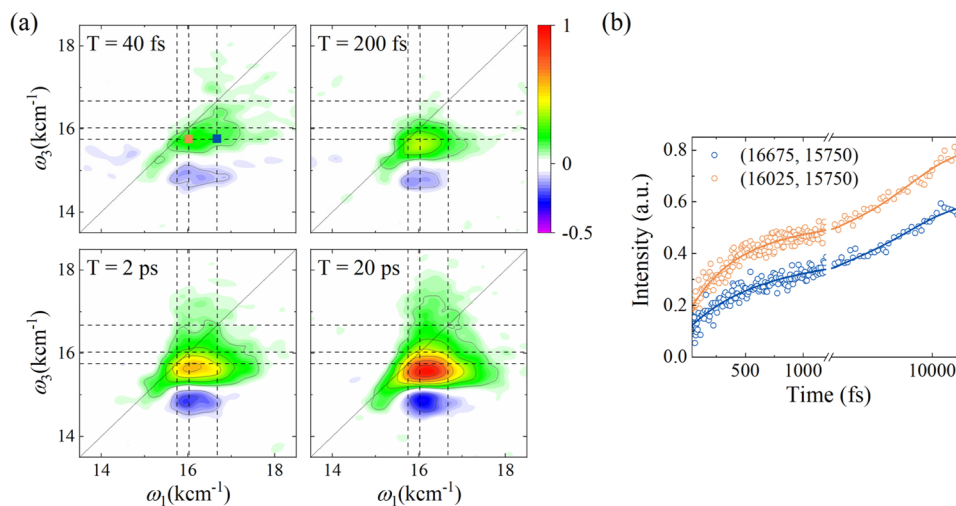
FIG. 4. (a) Polarization associated spectra (S_Y) recorded at the waiting times of T = 40 fs, 200 fs, 2 ps, and 20 ps with dashed lines indicating the excitonic energy levels. (b) The energy transfer kinetics from 40 fs to 20 ps at the cross-peaks in S_Y after intensity normalization. The global fits (lines) with a two-exponential fitting (including a non-decay component) $f(t) = \sum_{i=1}^{2} A_i \exp(-t/\tau_i)$ are superimposed on the raw data (dots), where τ is lifetime constant and A is the corresponding coefficient. The parameters are listed in Table I. The blue dots and line indicate the data for (16 675, 15 750 cm^{-1}), while the orange dots and line indicate the data for (16 025, 15 750 cm^{-1}), corresponding to the positions of peaks marked with squares with the same color in (a).

characteristics with that of $S_{\parallel}$ due to the severe spectral broadening. In contrast, the spectral congestion in S_Y is significantly suppressed, with signals predominantly distributed at cross-peaks, indicating a clearer feature of the EET process. As depicted in Fig. 4(b), the signal intensities at cross-peaks grow gradually over time, reaching its maximum at around 20 ps and beginning to decay after around 25 ps (Fig. S11 of the supplementary material). Lifetime analysis of the two cross-peaks at (16 675, 15 750 cm^{-1}) and (16 025, 15 750 cm^{-1}) by two-exponential fitting (Table I) yields two lifetime constants of 550 fs, 6.6 ps and 350 fs, 6.2 ps, respectively, which reflect the lifetime of the EET process. Based on the distance of the inter-pigment spacing, we attribute the ultrafast 300–500 fs component to the EET process from α84 to the adjacent β84, while the 6.6 ps component corresponds to the EET process within the monomer from β155 to β84. The latter significantly differs from previous estimated results (50 ps[26,27]) but more closely matches the rapid energy flow and equilibration observed in the PC rod (1–10 ps[29,30]). Obviously, the direct measured EET processes with time constants of 300–500 fs and 6.6 ps by polarization-controlled broadband 2DES agree with those by global fitting analysis of sliced 1D spectra from 2DES at selected excitation wavelengths for individual β155, α84, and β84. Furthermore, these EET rates are also consolidated by the femtosecond broadband transient fluorescence experiment, as detailed in S9 of the supplementary material.

B. Vibrational coherences

Apart from the EET kinetics, pronounced oscillatory features especially within the first 1 ps time window were observed, as depicted in Fig. 2(b). These oscillatory signals arise from the evolution of wavepackets initially excited by the broadband pulses and

TABLE I. Parameters in the global fits of the kinetics at cross-peaks (16 675, 15 750 cm^{-1}) and (16 025, 15 750 cm^{-1}) in S_Y. The third lifetime is set as infinity.

	A_1	τ_1 (fs)	A_2	τ_2 (ps)
(16 675, 15 750)	-0.21 ± 0.03	550 ± 150	-0.33 ± 0.03	6.6 ± 2.1
(16 025, 15 750)	-0.27 ± 0.03	350 ± 85	-0.37 ± 0.03	6.2 ± 1.7

display considerable intensity, exceeding 10% of the population signals. Through subtracting the population relaxation via multi-exponential global fitting of the 2D spectra, the oscillatory residues were obtained and then Fourier transformed with respect to T to determine the coherence frequency. The amplitude distribution of each coherence frequency, as a function of excitation and detection frequencies, makes up the FT coherence maps. The FT frequencies of the real rephasing signals are labeled as ω_T, and the integrated FT spectrum from 80 fs to 1.2 ps over ω_1 and ω_3 is shown in Fig. 5(a), top panel. The peak frequencies (ω_T = 210, 271, 468, 505, 666, 806, 873, 1048, 1234, 1378, 1574, and 1643 cm^{-1}) are consistent with those vibrational modes when compared to the known vibrational modes of the PC rod measured via difference fluorescence line-narrowing (ΔFLN) experiments, as well as the Raman spectra of PCB pigment.[28,58] Although there are slight discrepancies between frequencies observed in ultrafast transient experiments and those from vibrational spectroscopy, these differences fall within the experimental resolution of 28 cm^{-1}. The complex-valued residues are obtained by simultaneously subtracting the population decay from both the real and imaginary parts of 2D spectra. Applying FT to the complex-valued residues yields FT coherence maps with
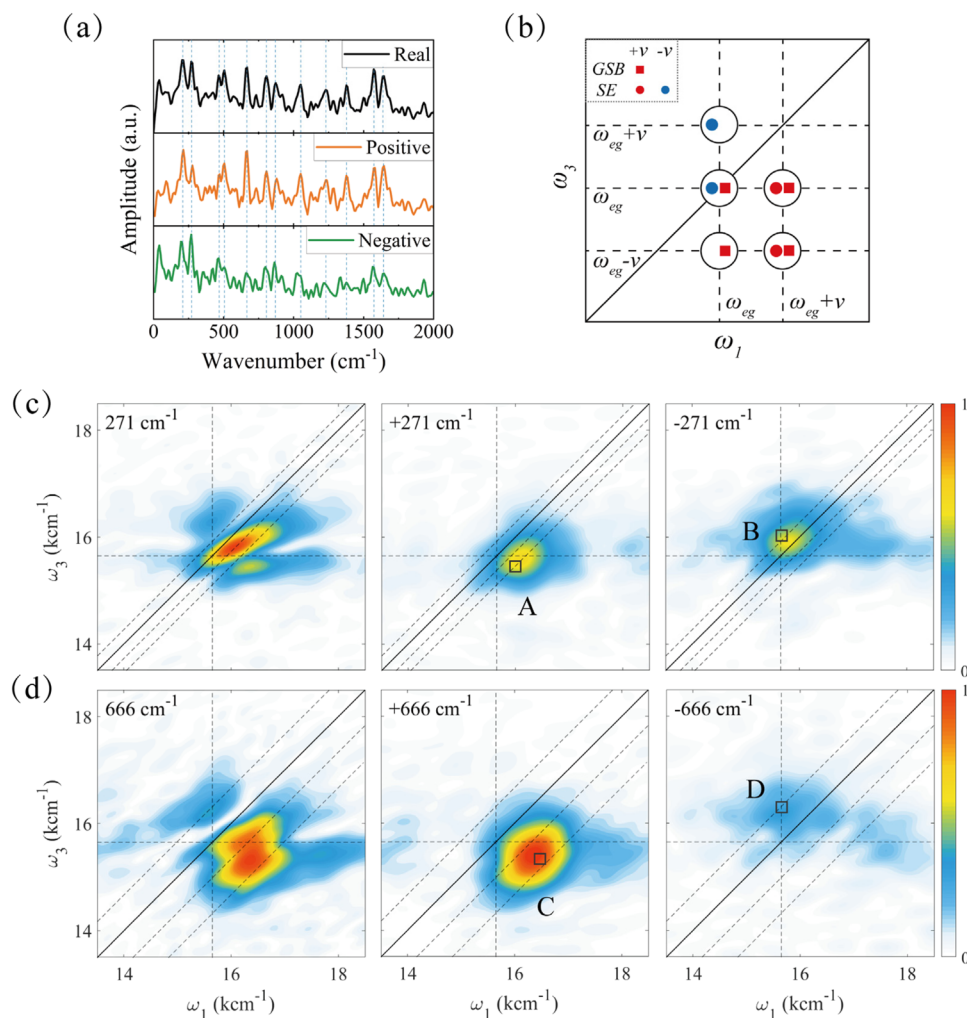
FIG. 5. (a) The integrated coherence spectra from 2D rephasing spectra from 80 fs to 1.2 ps. (b) Schematic diagrams of rephasing FT maps for vibrational coherence in the displaced harmonic oscillator system, where ω_{eg} is the $S_0–S_1$ transition energy and v is the coherent vibrational mode. (c) and (d) Real-value and complex-value rephasing Fourier transform coherence maps for the oscillation frequencies of 271 and 666 cm^{-1}, respectively. The vertical/horizontal line indicates the 0–0 transition of PC$_{620}$ at 15 650 cm^{-1}. The dashed lines parallel to the diagonal are offset from the diagonal by $\pm\omega_T$ and $+2\omega_T$.

positive and negative frequencies, $+\omega_T$ and $-\omega_T$. The integrated FT spectra are shown in Fig. 5(a), middle and bottom panels. The better S/N and higher intensity of $+\omega_T$ than $-\omega_T$ is because that there are more Liouville paths contributing to the positive frequencies.[59] In addition, according to the Feynman diagram, the positive and negative frequencies mainly originate from the ground and excited states, respectively.[59] A detailed comparison between $+\omega_T$ and $-\omega_T$ in Fig. S14 and Table S4 of the supplementary material reveals that the frequencies of most excited-state vibrational modes have a red shift relative to those of the ground state. Similar phenomena have been observed in the excited states of some dye molecules.[44,60,61]

Here, we mainly focus on the FT coherence maps of vibrational modes at 271 and 666 cm^{-1}. The corresponding FT coherence maps are shown in Figs. 5(c) and 5(d). The real-value FT coherence maps are plotted in the left panels, and the complex-value FT coherence maps are plotted in the middle and right panels. Both FT coherence maps of -271 and -666 cm^{-1} exhibit a broaden peak covering the diagonal peak and upper cross-peak. In the FT coherence maps of $\omega_T = +271$ and $+666$ cm^{-1}, a broaden peak is observed at the lower cross-peak. The lifetime of the vibrational wavepackets contributing to these two peaks can be estimated using the time–frequency transform (TFT) method based on the smoothed-pseudo-Wigner–Ville (SPWV) distribution.[62] TFT analysis is capable of extracting the main frequency components and their time behavior simultaneously. The results of TFT analysis represented in Fig. S16 of the supplementary material show the similar dephasing time of 200–300 fs for the mode at 271 cm^{-1} from the

ground state and excited state, as well as the similar dephasing time of 400–500 fs for the mode at 666 cm^{-1}.

Previous theoretical studies and experiments have shown that FT coherence maps are effective tools for distinguishing electronic, vibrational, and exciton–vibrational coherences.[59,63] Pure electronic coherence in the electronic dimer model mainly distributes on the symmetric off-diagonal peaks. However, it usually survives for less than 100 fs at ambient temperature.[14,16] Thus, it is excluded in PC$_{620}$ because we do not observe any large-amplitude coherent component decaying that fast as shown in Fig. 2(b). The pure vibrational coherence in a displaced harmonic oscillator (DHO) system exhibits a chair pattern as shown in Fig. 5(b), with four positive peaks from the excited and ground states forming a square pattern at the lower cross-peak and two negative peaks from the excited states locate on the diagonal peak and the upper cross-peak separated by an energy spacing of ω_T.[59] In our case, FT coherence maps of 271 cm^{-1} comply with the pattern predicted in the DHO model, as shown in Fig. 5(c). Peak A and peak B display approximately equal amplitudes, although the anticipated four peaks in the lower cross-peak and the two peaks in the upper cross-peak merge into a single broaden peak, respectively, due to spectral broadening and the narrow energy gap. This pattern suggests that the mode at 271 cm^{-1} originates from the pure vibrational coherence, as the FT coherence maps of exciton–vibrational coherence exhibit an asymmetric amplitude enhancement of the lower cross-peak.[64] The FT coherence maps of 666 cm^{-1} also manifest as two broaden peaks, one at the lower cross-peak and the other on the upper cross-peak, similar to that of 271 cm^{-1}. However, the lower cross-peak amplitude, denoted as peak C in Fig. 5(d), is ~threefold larger than that of peak D. We suggest that the amplitude enhancement of the lower cross-peak can be attributed to the predominance of ground-state coherence under excitation conditions. The coherence map node lines at the diagonal peak, which separate the signals above and below the diagonal in the real-value FT coherence maps [left panels of Figs. 5(c) and 5(d)], arise from the destructive interference between overlapping GSB and SE Liouville pathways. The node line separates the vibronic modes at the excited states from the pure vibrational modes at the ground states.[65] If there exists resonant exciton–vibrational coupling, the vibronic modes will undergo fast dephasing of the wavepackets,[13,66] leading to the disappearance of the real-value FT coherence map node line. Therefore, the appearance of the node line, together with the similar lifetime of the ground-state and excited-state wavepackets revealed by TFT analysis, is the indicator for the absence of the exciton–vibrational coupling in PC$_{620}$. The FT coherence maps and the lifetime analysis of other vibrational modes are shown in Figs. S15 and S16 of the supplementary material. All the FT maps show similar characteristics as those in the FT coherence maps of 271 and 666 cm^{-1}. Our results suggest that all the vibrational modes originate from the vibrational coherence and exclude the exciton–vibrational coupling between the adjacent α84 and β84 pigment pair.

To confirm the coherent signals, we conducted the HD-TG experiment using the same experimental setup with that of 2DES except for fixing the time delay between the first two pulses as 0. The residues of HD-TG are shown in Fig. 6(a), which reveal obvious oscillatory signals. Figure 6(b) represents the distribution of the vibrational modes along ω_3 (upper panel) as well as the integrated FT spectrum over ω_3 (lower panel). The FT spec-
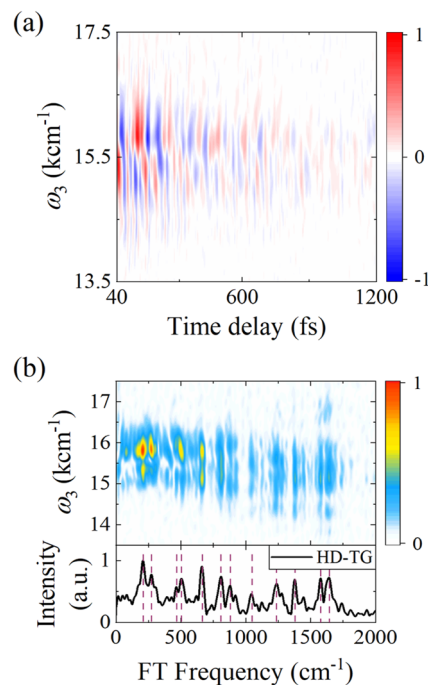

FIG. 6. (a) The residue spectra of HD-TG after subtracting the population decay by global fitting. The detected coherent dynamics are in the range of 40 fs–1.6 ps against the emission frequency ω_3. (b) Corresponding FT map of (a) from 80 fs to 1.6 ps (top), the coherence spectrum integrated along ω_3 (bottom).

trum of HD-TG at perpendicular polarization (see Fig. S17 of the supplementary material) reveals nearly the same coherent signals as those at parallel polarization. In addition, the BBTA experiment was also conducted and revealed an identical coherence spectrum (Fig. S18 of the supplementary material). Both HD-TG and BBTA detect the same impulsive Raman modes as those in 2DES, while these two spectroscopic methods help confirm those weak oscillatory signals in 2DES with a significantly shorter acquisition time and a higher S/N; however, these two methods cannot distinguish the excited-state vibrational frequencies from those of the ground state.

C. Solvation dynamics

The solvation response of protein–chromophore systems is of particular interest because the system–bath interaction has a significant impact on EET process.[1,67,68] The solvation dynamics of PC$_{620}$ and its α-subunit have been investigated using transient hole-burning experiments by Beck et al., revealing a red shift of the signals within 50 fs and a line broadening of the GSB and SE holes at around 200 fs, which were attributed to protein-matrix solvation dynamics and intramolecular vibrational redistribution.[56,69,70] Here, we aim to analyze the solvation response with a higher time resolution. As shown in Fig. 2(a), variations in peak shapes in 2DES at different T reflect the evolution of the system. As we discussed before, the changes in peak intensities and positions are related to the EET process of the system, while the changes in line shapes reflect the
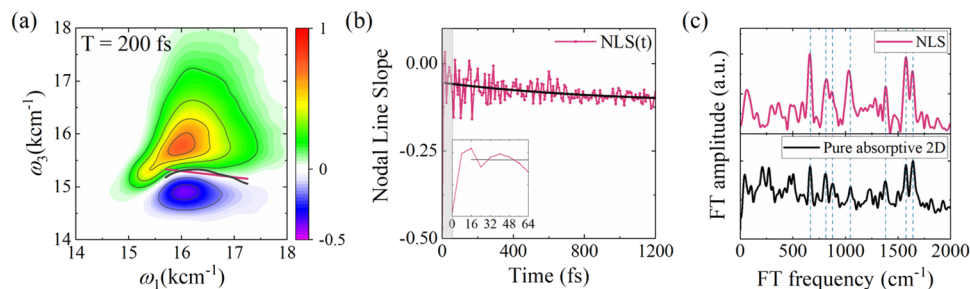
FIG. 7. (a) Nodal line (dark gray line) and the fitted nodal line slope (NLS, pink line) in the excitation wavelength range 15 700–17 250 cm^{-1}. (b) NLS(t) as a function of waiting time (pink dots and line) from 0 fs to 1.2 ps. Lifetime constant, $\tau \approx 900$ fs, is obtained by conducting single exponential fitting (black line) to the NLS(t). The inset at lower-left corner shows NLS(t) within 64 fs (gray shade), indicating that NLS rapidly relaxes within 16 fs. (c) Top, coherence spectra of the residual of NLS(t) from 16 fs to 1.2 ps. Bottom, coherence spectra of the pure absorptive 2D spectra from 80 fs to 1.2 ps. The blue vertical dashed lines mark the dominate modes that are the same in two coherence spectra.

interaction between the system and the environment, which can also be quantitatively analyzed in 2DES. The commonly used methods to extract solvation dynamics from 2DES include nodal line slope (NLS), dynamical Stokes shift, central line slope (CLS), and contour eccentricity.[42,71–73] These measurements are equivalent to the frequency fluctuation correlation function (FFCF) within the framework of linear response.[42]

The nodal line [gray line in Fig. 7(a)] demarcates the boundary between the positive and negative peaks, and the fitted NLS is shown as the pink line in Fig. 7(a). Nodal line dynamics serves as a marker for assessing the degree of the inhomogeneity due to spectral diffusion, thereby providing insights into the solvation time scales. Figure 7(b) shows the evolution of NLS over time within the excitation wavelength range of 15 700 to 17 250 cm^{-1}, the main signal distribution area. NLS undergoes rapid changes within just 16 fs, totally in the laser pulse overlapping temporal region. This phenomenon indicates that the system's inertial solvation response completes within 16 fs. Single-exponential fitting applied to NLS dynamics spanning from 16 fs to 1.6 ps yields a solvation lifetime of ~900 fs, corresponding to the diffusive solvation response. After subtracting population dynamics, significant oscillatory signals are unveiled in the residuals. Through performing FT of the residue of NLS(t) from 16 to 1200 fs, a series of vibrational modes are identified [Fig. 7(c), top]. Comparing with the FT frequencies extracted from the real part of the pure absorptive 2D signals along T, we find that the FT frequencies in NLS and pure absorptive 2D signals are essentially the same, except for minor discrepancies in relative intensity.

The spectral diffusion process is fundamentally linked to the system's energy relaxation and interaction with environment. The energy relaxation of excited states is attributed to the intramolecular and intermolecular interactions and solvent reorganization. The system is initially excited to vibronic states, subsequently undergoing a vibrational relaxation process whereby energy is dissipated to the surrounding bath through the vibrational cooling mechanism. Meanwhile, solvent molecules undergo rearrangement in response to the charge redistribution triggered by the excitation of the system. Although it is still under debate whether the proteins

or the solvent molecules dominate the solvation response, it has been experimentally confirmed that reorganization energy, scaffold proteins, and solvent molecules are closely related to the rate of solvation response.[57] In our case, we observe an extremely fast inertial response. It is mainly attributed to the inertial response of the solvent molecules because of smaller inertial moments. The large reorganization energy of the pigments in PC$_{620}$, which indicates a strong solvation capacity, also contributes to the inertial response.[38] Theoretical simulations and certain experiments have also confirmed that PC$_{620}$ has a faster solvation process than APC.[19,38] We suggest that it can be attributed to the more distorted configuration of $\alpha 84$ and $\beta 155$ located on the outer circumference in PC$_{620}$, which assist substantial access of water to where the pigments are bound and further induce a stronger system–bath interaction. The effects of system–bath interaction and those of inter-pigment coupling are largely in competition. Thus, the strong system–bath interaction facilitates the dephasing of the coherence. This aligns with the rapid dephasing rate of the vibrational modes, with lifetimes ranging from around 100 fs to 500 fs, as listed in Table S5 of the supplementary material. These rates in PC$_{620}$ are almost twice as fast as those in other algae light-harvesting proteins comprising PCB pigments such as PC577 and PC630.[74] Ultrafast energy dissipation via vibrational modes can be detected by the FT spectra of NLS and dynamical Stokes shift. We observed nearly all the vibrational modes appearing in the NLS [Fig. 7(c), top] and dynamical Stokes shift spectra probed at $\omega_1 = 15\,850$ cm^{-1} (Fig. S19 of the supplementary material), as those in the 2DES coherence spectrum [Fig. 7(c), bottom]. These oscillations originate from the coherent coupling of vibrational modes to electronic states as a wavepacket and are assigned to intramolecular vibrational modes of PC$_{620}$. According to our previous research, the resonant delocalized collective modes coupled to the exciton do not participate in the energy dissipation process due to quantum phase synchronization.[20] Therefore, the above phenomenon confirms the absence of exciton–vibrational coherence in PC$_{620}$, which also supports that the EET in PC$_{620}$ is incoherent. In addition, through fitting the dynamical Stokes shift with a damped sine function, the coherence lifetime in the energy dissipation process is estimated to be around 200 fs (Table S6 of the

supplementary material), much shorter than that observed in APC (500 fs), indicating a fast dephasing of the wavepacket without a protection effect by the quantum phase synchronization mechanism in the excitonic dimer.[20]

IV. CONCLUSION

We have investigated EET kinetics and vibronic effects in PC_{620} via 2DES at room temperature. With the global analysis of the 2DES data, we assigned the 460 fs decay component to the EET process from α84 to the adjacent β84, an 8.6 ps component from β155 to β84 and a 66 ps component from β155 to α84, respectively. When using polarization-controlled 2DES, the spectral broadening effect at the diagonal peaks in conventional 2DES is suppressed to highlight the EET signals at the cross-peaks. Thus, two EET components with lifetime constants of ~300–500 fs and 6.6 ps were directly resolved and assigned to EET from α84 to the adjacent β84 and from β155 to β84, respectively. These EET rates fully agree with those predicted by the FRET mechanism, while the CD spectrum also confirmed the absence of excitonic dimer in the adjacent α84–β84 pigment pair in PC_{620}. These preclude the possibility of delocalized coherent EET mechanism in PC_{620}, in contrast to that in APC. Beating signals in the kinetics are clearly distinguished as vibrational coherence via the FT coherence map pattern. By analyzing the FT spectra of NLS and dynamical Stokes shift, we showed that all the vibrational modes participate in the energy dissipation of the excited states, which again excluded the existence of the exciton–vibrational coherence. The twisted conformation of α84 is suggested to be responsible for the localized electronic states in PC_{620}, which are different from the delocalized states in APC. These findings unambiguously indicate that the incoherent EET mechanism plays a dominant role in PC_{620}. Our study provides insights into the incoherent photosynthetic mechanism and lays a foundation for future study on the highly efficient EET processes in the whole PBS.

SUPPLEMENTARY MATERIAL

See the supplementary material for additional sample preparation analysis, pulse characterization, x-ray structure of pigments in PC_{620} and APC, circular dichroism spectrum, global analysis, polarization-controlled 2DES, transient fluorescence experiment, FT spectra, FT coherence maps, time–frequency analysis, nodal line slope, and dynamics Stokes shift.

ACKNOWLEDGMENTS

AUTHOR DECLARATIONS

Conflict of Interest

The authors have no conflicts to disclose.

Author Contributions

Jiayu Wang: Data curation (lead); Formal analysis (lead); Investigation (lead); Methodology (equal); Visualization (lead); Writing – original draft (lead). **Ruidan Zhu**: Formal analysis (equal); Investigation (lead); Methodology (equal). **Jiading Zou**: Formal analysis (equal); Methodology (equal). **Heyuan Liu**: Data curation (equal); Methodology (equal). **Hanting Meng**: Formal analysis (supporting). **Zhanghe Zhen**: Formal analysis (supporting). **Wenjun Li**: Investigation (supporting); Resources (lead). **Zhuan Wang**: Investigation (supporting); Methodology (supporting). **Hailong Chen**: Investigation (supporting); Methodology (supporting). **Yang Pu**: Investigation (equal); Resources (lead); Supervision (equal). **Yuxiang Weng**: Conceptualization (lead); Formal analysis (lead); Methodology (lead); Supervision (lead); Writing – original draft (lead).

DATA AVAILABILITY

The data that support the findings of this study are available from the corresponding authors upon reasonable request.

REFERENCES

[1] Y.-C. Cheng and G. R. Fleming, Annu. Rev. Phys. Chem. **60**, 241 (2009).
[2] G. R. Fleming and G. D. Scholes, Nature **431**, 256 (2004).
[3] T. J. McGenity, B. A. McKew, and D. J. Lea-Smith, Nat. Microbiol. **6**, 419 (2021).
[4] S. V. Shestakov and E. A. Karbysheva, Biol. Bull. Rev. **7**, 259 (2017).
[5] T. Gillbro, A. V. Sharkov, I. V. Kryukov, E. V. Khoroshilov, P. G. Kryukov, R. Fischer, and H. Scheer, Biochim. Biophys. Acta, Bioenerg. **1140**, 321 (1993).
[6] G. W. Suter, P. Mazzola, J. Wendler, and A. R. Holzwarth, Biochim. Biophys. Acta, Bioenerg. **766**, 269 (1984).
[7] Th. Forster, "Intermolecular energy migration and fluorescence," Ann. Phys. **437**(1–2), 55–75 (1948).
[8] G. D. Scholes, Annu. Rev. Phys. Chem. **54**, 57 (2003).
[9] R. E. Blankenship, *Molecular Mechanism of Photosynthesis*, 3rd ed. (Wiley Blackwell, 2014).
[10] G. S. Engel, T. R. Calhoun, E. L. Read, T.-K. Ahn, T. Mančal, Y.-C. Cheng, R. E. Blankenship, and G. R. Fleming, Nature **446**, 782 (2007).
[11] E. Collini, C. Y. Wong, K. E. Wilk, P. M. G. Curmi, P. Brumer, and G. D. Scholes, Nature **463**, 644 (2010).
[12] C. Y. Wong, R. M. Alvey, D. B. Turner, K. E. Wilk, D. A. Bryant, P. M. G. Curmi, R. J. Silbey, and G. D. Scholes, Nat. Chem. **4**, 396 (2012).
[13] E. Thyrhaug, R. Tempelaar, M. J. P. Alcocer, K. Žídek, D. Bína, J. Knoester, T. L. C. Jansen, and D. Zigmantas, Nat. Chem. **10**, 780 (2018).
[14] R. Zhu, M. Ruan, H. Li, X. Leng, J. Zou, J. Wang, H. Chen, Z. Wang, and Y. Weng, J. Chem. Phys. **156**, 125101 (2022).
[15] G. D. Scholes, G. R. Fleming, L. X. Chen, A. Aspuru-Guzik, A. Buchleitner, D. F. Coker, G. S. Engel, R. van Grondelle, A. Ishizaki, D. M. Jonas, J. S. Lundeen, J. K. McCusker, S. Mukamel, J. P. Ogilvie, A. Olaya-Castro, M. A. Ratner, F. C. Spano, K. B. Whaley, and X. Zhu, Nature **543**, 647 (2017).
[16] H.-G. Duan, V. I. Prokhorenko, R. J. Cogdell, K. Ashraf, A. L. Stevens, M. Thorwart, and R. J. D. Miller, Proc. Natl. Acad. Sci. U. S. A. **114**, 8493 (2017).
[17] A. Chenu and G. D. Scholes, Annu. Rev. Phys. Chem. **66**, 69 (2015).
[18] J. Lim, D. Paleček, F. Caycedo-Soler, C. N. Lincoln, J. Prior, H. von Berlepsch, S. F. Huelga, M. B. Plenio, D. Zigmantas, and J. Hauer, Nat. Commun. **6**, 7755 (2015).
[19] J. M. Womick and A. M. Moran, J. Phys. Chem. B **113**, 15747 (2009).
[20] R. Zhu, W. Li, Z. Zhen, J. Zou, G. Liao, J. Wang, Z. Wang, H. Chen, S. Qin, and Y. Weng, Nat. Commun. **15**, 3171 (2024).
[21] A. N. Glazer, Ann. Rev. Biophys. Biophys. Chem. **14**, 47 (1985).
[22] J. Pieper, M. Rätsep, M. Golub, F.-J. Schmitt, P. Artene, and H.-J. Eckert, Photosynth. Res. **133**, 225 (2017).

[23] C. Theiss, F.-J. Schmitt, J. Pieper, C. Nganou, M. Grehn, M. Vitali, R. Olliges, H. J. Eichler, and H.-J. Eckert, J. Plant Physiol. **168**, 1473 (2011).

[24] S. Sil, R. W. Tilluck, N. Mohan, T. M, C. H. Leslie, J. B. Rose, M. A. Domínguez-Martín, W. Lou, C. A. Kerfeld, and W. F. Beck, Nat. Chem. **14**, 1286 (2022).

[25] S. Sohoni, L. T. Lloyd, A. Hitchcock, C. MacGregor-Chatwin, A. Iwanicki, I. Ghosh, Q. Shen, C. N. Hunter, and G. S. Engel, J. Am. Chem. Soc. **145**, 11659 (2023).

[26] M. P. Debreczeny, K. Sauer, J. Zhou, and D. A. Bryant, J. Phys. Chem. **99**, 8420 (1995).

[27] M. P. Debreczeny, K. Sauer, J. Zhou, and D. A. Bryant, J. Phys. Chem. **99**, 8412 (1995).

[28] G. Gryliuk, M. Rätsep, S. Hildebrandt, K. D. Irrgang, H. J. Eckert, and J. Pieper, Biochim. Biophys. Acta, Bioenerg. **1837**, 1490 (2014).

[29] Y. Hirota, H. Serikawa, K. Kawakami, M. Ueno, N. Kamiya, and D. Kosumi, Photosynth. Res. **148**, 181 (2021).

[30] C. Nganou, L. David, N. Adir, and M. Mkandawire, Photochem. Photobiol. Sci. **15**, 31 (2016).

[31] N. Adir, Y. Dobrovetsky, and N. Lerner, J. Mol. Biol. **313**, 71 (2001).

[32] L. David, M. Prado, A. A. Arteni, D. A. Elmlund, R. E. Blankenship, and N. Adir, Biochim. Biophys. Acta, Bioenerg. **1837**, 385 (2014).

[33] K. Brejc, R. Ficner, R. Huber, and S. Steinbacher, J. Mol. Biol. **249**, 424 (1995).

[34] M. D. Edington, R. E. Riter, and W. F. Beck, J. Phys. Chem. **99**, 15699 (1995).

[35] M. D. Edington, R. E. Riter, and W. F. Beck, J. Phys. Chem. **100**, 14206 (1996).

[36] M. D. Edington, R. E. Riter, and W. F. Beck, J. Phys. Chem. B **101**, 4473 (1997).

[37] B. J. Homoelle, M. D. Edington, W. M. Diffey, and W. F. Beck, J. Phys. Chem. B **102**, 3044 (1998).

[38] J. M. Womick and A. M. Moran, J. Phys. Chem. B **113**, 15771 (2009).

[39] J. M. Womick and A. M. Moran, J. Phys. Chem. B **115**, 1347 (2011).

[40] E. Collini, Chem. Soc. Rev. **42**, 4932 (2013).

[41] B. K. Petkov, T. A. Gellen, C. A. Farfan, W. P. Carbery, B. E. Hetzler, D. Trauner, X. Li, W. J. Glover, D. J. Ulness, and D. B. Turner, Chem **5**, 2111 (2019).

[42] J. Lu, Y. Lee, and J. M. Anna, J. Phys. Chem. B **124**, 8857 (2020).

[43] F. D. Fuller and J. P. Ogilvie, Annu. Rev. Phys. Chem. **66**, 667 (2015).

[44] R. Zhu, J. Zou, Z. Wang, H. Chen, and Y. Weng, J. Phys. Chem. A **124**, 9333 (2020).

[45] E. Thyrhaug, T. J. Sørensen, I. Gryczynski, Z. Gryczynski, and B. W. Laursen, J. Phys. Chem. A **117**, 2160 (2013).

[46] E. Thyrhaug, K. Žídek, J. Dostál, D. Bína, and D. Zigmantas, J. Phys. Chem. Lett. **7**, 1653 (2016).

[47] A. C. Albrecht, J. Mol. Spectrosc. **6**, 84 (1961).

[48] Y.-x. Weng, Chin. J. Chem. Phys. **31**, 135 (2018).

[49] J. Zou, R. Zhu, J. Wang, H. Meng, Z. Wang, H. Chen, and Y.-X. Weng, J. Phys. Chem. Lett. **14**, 4657 (2023).

[50] R. Zhu, S. Yue, H. Li, X. Leng, Z. Wang, H. Chen, and Y. Weng, Opt. Express **27**, 15474 (2019).

[51] T. Schirmer, W. Bode, and R. Huber, J. Mol. Biol. **196**, 677 (1987).

[52] J. Nield, P. J. Rizkallah, J. Barber, and N. E. Chayen, J. Struct. Biol. **141**, 149 (2003).

[53] L. Zheng, Z. Zhang, H. Wang, Z. Zheng, J. Wang, H. Liu, H. Chen, C. Dong, G. Wang, Y. Weng, N. Gao, and J. Zhao, Nat. Commun. **14**, 3961 (2023).

[54] M. P. Debreczeny, K. Sauer, J. Zhou, and D. A. Bryant, J. Phys. Chem. **97**, 9852 (1993).

[55] I. H. M. van Stokkum, D. S. Larsen, and R. van Grondelle, Biochim. Biophys. Acta, Bioenerg. **1657**, 82 (2004).

[56] R. E. Riter, M. D. Edington, and W. F. Beck, J. Phys. Chem. B **101**, 2366 (1997).

[57] C. C. Jumper, P. C. Arpin, D. B. Turner, S. D. McClure, S. R. Rather, J. C. Dean, J. A. Cina, P. A. Kovac, T. Mirkovic, and G. D. Scholes, J. Phys. Chem. Lett. **7**, 4722 (2016).

[58] F. Andel, J. T. Murphy, J. A. Haas, M. T. Mcdowell, I. van der Hoef, J. Lugtenburg, J. C. Lagarias, and R. A. Mathies, Biochemistry **39**, 2667 (2000).

[59] V. Butkus, D. Zigmantas, L. Valkunas, and D. Abramavicius, Chem. Phys. Lett. **545**, 40 (2012).

[60] S. R. Rather and G. D. Scholes, J. Phys. Chem. A **120**, 6792 (2016).

[61] S. R. Rather, J. C. Dean, and G. D. Scholes, J. Phys. Chem. A **119**, 11837 (2015).

[62] A. Volpato and E. Collini, Opt. Express **23**, 20040 (2015).

[63] V. R. Policht, A. Niedringhaus, and J. P. Ogilvie, J. Phys. Chem. Lett. **9**, 6631 (2018).

[64] V. Tiwari, W. K. Peters, and D. M. Jonas, Proc. Natl. Acad. Sci. U. S. A. **110**, 1203 (2013).

[65] A. Sahu and V. Tiwari, J. Phys. Chem. Lett. **14**, 4617 (2023).

[66] S.-H. Yeh, R. D. Hoehn, M. A. Allodi, G. S. Engel, and S. Kais, Proc. Natl. Acad. Sci. U. S. A. **116**, 18263 (2019).

[67] M. Mohseni, P. Rebentrost, S. Lloyd, and A. Aspuru-Guzik, J. Chem. Phys. **129**, 174106 (2008).

[68] M. B. Plenio and S. F. Huelga, New J. Phys. **10**, 113019 (2008).

[69] R. R. Riter, M. D. Edington, and W. F. Beck, J. Phys. Chem. **100**, 14198 (1996).

[70] B. J. Homoelle and W. F. Beck, Biochemistry **36**, 12970 (1997).

[71] R. E. Wood, L. T. Lloyd, F. Mujid, L. Wang, M. A. Allodi, H. Gao, R. Mazuski, P.-C. Ting, S. Xie, J. Park, and G. S. Engel, J. Phys. Chem. Lett. **11**, 2658 (2020).

[72] F. Šanda, V. Perlík, C. N. Lincoln, and J. Hauer, J. Phys. Chem. A **119**, 10893 (2015).

[73] K. Kwac and M. Cho, J. Phys. Chem. A **107**, 5903 (2003).

[74] C. C. Jumper, I. H. M. van Stokkum, T. Mirkovic, and G. D. Scholes, J. Phys. Chem. B **122**, 6328 (2018).

22 August 2024 13:05:30